Optimization of spatial resolution and scattering effects for biomedical fluorescence imaging by using sub-regions of the shortwave infrared spectrum

*Benjamin Musnier[1], Maxime Henry[1], Julien Vollaire[1], Jean-Luc Coll[*1], Yves Usson[2], Véronique Josserand[1], Xavier Le Guével[1*]*

[1] Cancer Targets & Experimental Therapeutics, Institute for Advanced Biosciences (IAB), University of Grenoble Alpes (UGA)/ INSERM-U1209 / CNRS-UMR 5309 Grenoble, France
[2] TIMC-IMAG, University of Grenoble Alpes, CNRS-UMR 5525, Grenoble, France

E-mail: xavier.le-guevel@univ-grenoble-alpes.fr

Keywords: shortwave infrared, fluorescence imaging, gold nanoclusters, tissue penetration, scattering

Abstract

We evaluated the impact of light-scattering effects on spatial resolution in different SWIR sub-regions by analyzing two SWIR emissive phantoms made of PDMS-gold nanoclusters (Au NCs) composite covered with mice skin, or capillary tubes filled with Au NCs or IRDye 800CW at different depth in intralipids and finally, after administration of the Au NCs intravenously in mice.

Our findings highlighted the benefit of working at the highest tested spectral range of the SWIR region with a 50% enhancement of spatial resolution measured in artificial model when moving from NIR-II (1000- 1300 nm) to NIR-IIa (1300-1450 nm) region, and a 25% reduction of the scattering from the skin determined by point spread function analysis from the NIR-II to NIR-IIb region (1500-1700 nm). We also confirmed that a series of Monte Carlo restoration of images significantly improved the spatial resolution *in vivo* in mice in deep tissues both in the NIR-II and NIR-IIa spectral windows.

Introduction

In vivo fluorescence optical imaging has been widely developed during the last decades in preclinical studies with successful translation toward clinics, in particular for optical guided surgery[1-3]. The visible (400-700 nm) and NIR-I (700-900 nm) optical windows were initially used due to the availability of: i) a large library of commercial or easily synthesizable fluorophores, ii) highly sensitive silicon detectors and, iii) powerful lasers or light emitting diodes (LEDs) available in a wide range of wavelengths. The very high sensitivity of this imaging modality allows molecular imaging with insights of biological features at the cellular level[4]. However, these spectral windows still present severe limitations to achieve both high sensitivity and spatial resolution deep in biological tissues due to the substantial light absorption, high scattering and, autofluorescence of endogenous components[1, 5].

This initiated the search for other spectral windows where these limiting factors would be further reduced. It resulted in considerably improved contrast and spatial resolution, achieved in the shortwave infrared (SWIR) region, also called NIR-II, between 900 and 1700 nm[6]. Since the seminal works of Hongjie Dai's team exploring the SWIR window for biomedical applications in the early 2010's[7-10], major progresses in this new optical window have occurred on three key aspects.

Firstly, the transition from NIR-I to SWIR imaging window has been made possible by the significant advances on indium–gallium–arsenide (InGaAs) camera technology and associated optics. This yielded to affordable detection systems with high sensitivity between 900 nm and 2100 nm and an efficient noise reduction using thermoelectric cooling systems[11].

Secondly, the rapid development of bright SWIR probes made of organic[12] and inorganic materials such as quantum dots[13-15], lanthanide nanoparticles[16, 17], and metal nanoclusters[18-20] has contributed to improve the sensitivity of detection in artificial models and also *in vivo* in small animals. For example, ultra-small gold nanoparticles with diameters smaller than 3 nm, namely gold nanoclusters (Au NCs), have shown relatively high quantum yields with photoluminescence that could be detected above 1250 nm accompanied with a renal clearance when injected in mice[18, 20].

Recently, FDA-approved or at clinical stage contrast agents emitting mainly in the NIR-I and belonging to the cyanine family, like ICG or IRDye 800CW, have been employed for SWIR imaging to envision moving forward to the clinic[21-23] with a first human study reported in 2020[2].

Lastly, imaging processing and reconstruction have been extensively used in most of the biomedical imaging techniques in order to improve image quality and to extract physio-pathological data. For instance, it has been shown that imaging reconstruction based on Monte Carlo restoration of SWIR images could enhance by 59% the spatial resolution and by one order of magnitude the contrast. This enabled to identify non-invasively subtle vascular disorders in bone morphogenetic protein 9 (*Bmp9*)-deficient mice[20].

While SWIR imaging has shown obvious improvement compared to visible and NIR-I optical windows, there is still a lack of studies quantifying the influence of scattering as a function of penetration depth in biological tissues in different SWIR sub-regions.

In this work, we developed and characterized a SWIR imaging system for non-invasive small animal imaging *in vivo* and we investigated the use of two different contrast agents: Au NCs[20] and IRDye 800CW[21] first in artificial models and then *in vivo* in mice.

The first artificial model used to study scattering effects was based on a PDMS/AuNCs composite SWIR emitting bulk covered by a mouse skin flap. The changes observed between the different SWIR sub-regions on scattering point-spread function highlighted a drastic reduction of light scattering at higher wavelengths. This model allowed to obtain robust and complete results with quantitative data, moving one step further to *in vivo* scattering mimicking.

The second artificial model consisted in capillary tubes filled with various concentrations of contrast agents immerged in a 2% intralipid solution, mimicking blood vessels at different depths in strongly scattering tissues. Analyses of these capillary tubes in the NIR-I region and in several SWIR sub-windows, supported the benefit of moving throughout the SWIR window in terms of spatial resolution. Indeed, we show that below 4 mm of intralipid, the higher the fluorescence signal was collected, the more accurately the capillary spatial geometry was reported.

Finally, these findings were validated *in vivo* by imaging a mouse perfused with Au NCs in different SWIR sub-windows, supporting the remarkable improvement in vascular network visualization with enhanced-spatial resolution in depth when collecting a fluorescence signal above 1500 nm and after image processing using a Monte Carlo restoration.

Materials and methods:

Materials. Indocyanine Green (ICG) was purchased from Serb®. IRDye 800CW was purchased from LI-COR Biosciences. Sylgard® 184 Silicone Elastomer was purchased from Neyco S.A. Brand silicone 10 to 1 encapsulants were supplied as two-part liquid component kits. When

liquid components were thoroughly mixed, the mixture cured to a flexible elastomer. Fine bore polythene tubing were purchased from Smiths medical. Emulsion of intralipid 20% which is a lipid emulsion comprising soybean oil was purchased from Merck-France. The intralipid 2% solution was obtained by diluting 10 times the commercial solution in deionized water. All other chemicals and biological reagents were purchased from Merck.

Synthesis of Au NCs. We slightly modified a protocol described by Musnier *et al.*[19] to produce the SWIR-emitted Au NCs using the initial molar ratio Au: Ligand = 1:4. Briefly 250 µL of $HAuCl_4.3H_20$ (20 mM) was added to 4.8 mL water followed by 4 mL of the thiolated ligand mixture mercaptohexanoic acid (MHA, 5 mM)) / tetra(ethyleneglycol)dithiol (TDT, 5 mM) with a volume ratio MHA/TDT= 3 mL/1 mL. The color of the solution changed from yellowish to slightly pale cloudy. After 5 minutes, 250 µL of NaOH (1M) was added dropwise leading to almost colorless sols. After 5 minutes, 150 µL $NaBH_4$ (20 mM in 0.2M NaOH) was introduced dropwise under mild stirring and kept under stirring at 350 rpm for 8 hours. Purification of the Au NCs on 3 kDa cut-off filter column (Amicon) was repeated 3 times to stop the reaction and solutions were kept stored in the fridge until the experiments.

SWIR imaging platform. The imaging system was made of two parts with the excitation and the collection systems as illustrated in **Figure 1a**. The excitation sources consisted of 8 LEDs at 730 nm and 830 nm (4 per wavelength) mounted on a metal ring (Opto) at 30 cm working distance. Each LED was coupled to a ground glass, acting as a homogenizer, a collimator (Opto) and a set of short-pass (SP) filters (SP 750 nm, SP 850nm (Thorlabs), SP 1150 nm (Edmund Optics)) extinguishing unwanted parasite wavelengths. The LED_{730nm} excitation yielded a beam with an irradiance of 16 mW/cm^2 on a 30 cm^2 area and the LED_{830nm} excitation yielded a beam with an irradiance of 68 mW/cm^2 on a 23 cm^2 area (**Figure 1b**). Photons were collected through a set of long-pass (LP) filters (LP Colored 850 nm (Thorlabs)) and LP1064 nm (Semrock)) followed by interchangeable long-pass filters (Thorlabs) delineating four SWIR imaging sub-regions (1064 nm-1700 nm for LP1064 nm; 1250 nm-1700 nm for LP1250 nm; 1300 nm-1700 nm for LP1300 nm; 1500 nm-1700 nm for LP1500 nm) (**Figure 2d**).

The filtered light was focused on an InGaAs camera chip (NIRvana 640ST, 640 x 512 array, 900 nm to 1700 nm (Princeton)) using fixed focal length lenses (Navitar) of 25 mm (Field of view (FOV): 114 mm x 91 mm) or 50 mm (FOV: 43mm x 34 mm). The InGaAs camera was cooled to -60 °C, the analog to digital (AD) conversion rate was set to 2 MHz to have the highest image quality, the gain was set to "high", and different exposure times were selected to reach

about 50% of the dynamic range of the camera (0-46000 gray levels). All SWIR images were background corrected using LightField imaging software® (Princeton).

NIR-I imaging. Experiments were performed with a NIR 2D-Fluorescence reflectance-imaging device (Fluobeam 800®, Fluoptics, France). The excitation was provided by a class 1 expanded laser source at 780 nm and the irradiance on the imaging field was 10 mW/cm^2. A CCD camera (696 x 576 array, 300 to 1000 nm, FOV: 127 mm x 95 mm) collected the fluorescence signal through a long pass filter (LP830 nm).

Contrast agents' fluorescence detectability. Drops of contrast agents (10 µL in PBS 10mM) at different concentrations were imaged through the 50 mm fixed focal length lens under 830 nm excitation source using adapted exposure times. The concentration linearity range (R^2 > 0.995) and the limit of detection (SNR > 3) on the 1064 nm–1700 nm region were determined for Au NCs and IRDye 800CW.

Composite Au NCs / PDMS artificial model. A mixture of the two liquids from Sylgard® 184 Silicone Elastomer component kit was poured in a homemade Fortal mold consisting of a small tank with a pillar inside. After air bubbles removing using a water pump, the mold was placed overnight in an oven (60°C). The PDMS bulk presented then a small tank with a volume of 1cm^3 where the contrast agent was embedded. This photoluminescent part was made of a mix of Au NCs lyophilized powder (90 mg), silicone elastomer (1 g) and curing agent (100 mg). After air bubbles removing using a water pump, the mold was placed overnight in an oven (60°C). After complete drying, the bulk edges were cut to reach a square of 2 cm by 2 cm and the top surface was homogenized using a Leica CM3050 S cryostat to remove surface irregularities. The composite bulk, apart from an emitting window of 5 mm by 5 mm on the top surface, was covered with black foil (Thorlabs) to avoid reflections and parasite scattering.
The composite Au NCs / PDMS bulk was imaged under the 830 nm excitation with the 25 mm fixed focal length lens before and after superposition of a skin flap taken from a BALB/c nude mouse (Janvier labs, France) as illustrated in **Figure 4a**. A set of 3 images was taken for each condition to perform robust and reproducible analysis.

Edge and point spread function data analysis. Multi-line cross-sectional intensity profile analysis of the emitting bulk was performed using ImageJ software. The profiles obtained also called edge spread functions (ESF) were then extracted to perform data treatment and analysis

through the software GNU Octave. A script was used to normalize these ESF before deriving them by calculating the difference between two adjacent values. The gathered functions, known as empirical point spread functions (empirical-PSF), were fitted by Gaussian functions to obtain fitted point spread functions (fitted-PSF). After normalization of the fitted PSF, the full width at half maximum (FWHM) was extracted using Origin Pro 7 software (Origin©) in order to compare the influence of SWIR sub-windows on scattering. In our study, ESF and PSF were used only to assess light-scattering that is much greater than the theoretical diffraction scattering of our lens (< 1 pixel).

Capillaries imaging. Effect of scattering on the spatial resolution was estimated using a fine bore polythene tubing (OD = 0.96 mm / ID = 0.58 mm; Portex) filled with Au NCs or IRDye 800CW and immersed in a 2% Intralipid[24, 25] solution (**Figure 1c**) at increasing depths between 1 and 8 mm.

Each condition was recorded through the 50 mm fixed focal length lens. The two contrast agents were excited at 730 nm and 830 nm for SWIR imaging (exposure time from 100 ms to 2s) and at 780 nm for NIR-I imaging (exposure time from 150 ms to 1s). Measurements were reproduced 3 times for each condition to perform robust and reproducible analyses.

Data analysis. Images analysis was performed using ImageJ software. Measurements of signal intensity were done in a define region of interest (ROI) manually located on the capillary without intralipid and kept unchanged for all intralipid heights. The noise was measured at the edge of images in an area without relevant signal. Signal to noise ratio (SNR) was calculated as the mean signal intensity from the capillary divided by the noise. An arbitrary threshold value of 3 was fixed as a limit for SNR. Below this value, we considered that the signal from the capillary was not significant.

To evaluate scattering effect on each image, a cross-sectional intensity profile of the capillary was performed using the plot profile module of imageJ software. The full width at half maximum (FWHM) evaluated by a fit of a Gaussian curve (Origin Pro 7 software) was obtained on each profile to describe the capillary width imaged by the camera for each condition. The FWHM or relative width obtained was compared with the real width of the capillary as a percentage defined as:

$$eq\ 1 : \% = fit\ FWHM{-}constructor\ width * 100.$$

***In vivo* mouse experiment.** A six weeks old NMRI nude female mouse (Janvier Labs, France) was anesthetized (air/isoflurane 4%) and a catheter (BD neoflon) was positioned in the tail vein. The femoral artery was then incised to let the blood flow out and Au NCs contrast agent (360 µM in PBS 1X) was perfused intravenously via the catheter. Exagon (1 mL/kg) was injected immediately after to sacrifice the mouse. Imaging was performed immediately after the sacrifice using the 830 nm excitation and the 50 mm fixed focal length lens.

Results

1- Fluorescence detectability of SWIR contrast agents

Contrast agents emitting in the visible or NIR-I optical windows have been widely studied and characterized in the last decades, using well-known and affordable silicon based detectors and spectrometers[26, 27]. SWIR-emitting contrast agents still remain poorly evaluated due to the short list of candidates as well as the rarity of *in vivo* SWIR imaging systems in research laboratories. In order to develop *in vivo* imaging followed by medical applications in the SWIR, recent works reported the ability to use cyanine dyes ICG and IRDye 800CW as SWIR contrast agents[2, 22, 28]. Despite moderate quantum yields (QY) in this optical window with photoluminescence (PL) from the tail of their emission spectra, these probes presented the advantage to be already clinically approved, thus being references for comparison of new SWIR contrast agents.

While ICG and IRDye 800CW offered similar absorbance profiles with a maximum at 775 nm in PBS buffer, Au NCs showed two NIR absorbance bands at 680 nm and 775 nm accompanied by a tail up to 1000 nm (**Figure 2a**). Au NCs exhibited a broader PL emission in the SWIR at longer wavelengths than IRDye 800CW and ICG as depicted in **Figures 2b and 2d**.

In this study we selected Au NCs and the cyanine dye IRDye 800CW as reference probe instead of ICG. In fact, by measuring the PL emission of a droplet and normalizing to the exposure time, we found IRDye 800CW 7 folds brighter in the SWIR than ICG at the same concentration in PBS (**Figure 2c**). Furthermore, IRDye 800CW presents the advantages of a high colloidal stability, a fast renal clearance[21, 28], and the ability to be conjugated to molecules of interest. Au NCs' PL was found more than 3 times higher than IRDye 800 CW'PL at the same concentration (**Figure 2c**), with the ability to excite them over a wide window of wavelengths (from 400 to 850nm) (**Figure 2d**) and a much higher photostability under NIR-I light exposure at 140 mW/cm^2 during 2 hours (**Figure S1**).

We first determined the sensitivity of detection of the two contrast agents (Au NCs and IRDye 800CW) in the SWIR (1064 nm-1700 nm) by measuring their PL at different concentrations. For IRDye 800 CW, the linear range of detection was estimated between 98 nM and 25 µM. Above 25 µM, fluorescence quenching occurred in both NIR-I and SWIR optical windows. For Au NCs, the signal was linear between 22 nM and 90 µM without any quenching at the highest concentration measured. At similar SNR ~5.5, the sensitivity of detection of Au NCs was 3 times better than for IRDye 800CW (89 nM and 391 nM respectively) (**Figure S2b, Table 1**).

Contrast agents	Limit of detection (LOD)	SNR at LOD
Au NCs	22±2 nM	4.43±0.22
IRDye 800CW	98±5 nM	3.05±0.15

Table 1. Sensitivity of detection in SWIR of Au NCs and IRDye 800CW solutions.

2- Optical scattering studies on phantom covered by a mouse skin flap in different SWIR sub-windows

A SWIR calibration tool was developed by mixing an elastomer and lyophilized Au NCs powder on a PDMS container. The composite bulk obtained presented a strong PL even at low exposure times on a large and homogeneous emitting area over the full SWIR range (50% of saturated signal at 50 ms exposure time using LP1500 nm). This highly PL emitting and precisely designed phantom allowed to study light scattering due to the skin with more sensitivity and accuracy. Thus, a skin flap with thickness between 2 to 3mm collected from a mouse's back was placed over the calibration tool as illustrated in **Figure 3a**. Scattering induced by the skin was studied in different SWIR sub-regions by measuring the changes on edge and point spread function (ESF and PSF).

Multi-line cross-sectional intensity profile analyses were performed on the side of the emitting bulk. By following the approach summarized in **Figure 3b**, it was possible to obtain FWHM of PSF for each SWIR sub-windows. In theory, a perfectly straight edge would lead, for the bulk without skin on top, to a rectangular function for ESF and thus a FWHM tending toward zero. Our bulk wasn't a perfectly straight-line and orthogonal block leading to the ESF shapes observed without skin.

The comparison of the normalized PSF Gaussian functions for the bulk covered or not by skin, as showed in **Figure 4a**, allowed to directly evaluate the impact of scattering from the skin. As

depicted in **Figure 4a**, the differences observed between the images obtained using different LPs indicated a decrease of diffuse scattering at longer wavelengths from a blurry image with LP1064 nm to a sharp one with LP1500 nm.

The FWHM of each normalized PSF Gaussian function was extracted to characterize the impact of scattering from the skin for the different LPs (**Figure 4b**). For instance, for the LP 1064 nm, we observed a FWHM of 4.7 pixels (pixel size: 70 µm * 70 µm) with skin versus 2.2 pixels (+113%) without skin. A relative comparison of results for the different SWIR LPs documents the important decrease of the FWHMs obtained with skin (- 25%, - 13% and - 8% for LP1250 nm, LP1300 nm and LP1500 nm compared to LP1064 nm) as well as a diminution of the differences between FWMH with and without skin (72%, 67% and 44% for LP1250 nm, LP1300 nm and LP1500 nm). The FWHM for the emitting bulk with skin decreased when using higher imaging wavelengths, highlighting a reduction of diffuse scattering and collection of more realistic images.

3- Wavelength collection range influences light scattering and impacts in-depth spatial resolution.

We present here the results obtained with Au NCs at the 830 nm excitation (**Figure 5**). Measurements performed under excitation at 730 nm and with IRDye 800CW are available in the supporting information (Figures S3, S4). Notably, for IRDye 800CW, we obtained a better sensitivity of detection in intralipids using 830 nm excitation instead of 730 nm which was quite beyond the maximum of absorption. This effect could be either due to a lower self-reabsorption from the organic dye or a deeper penetration of light at longer wavelength.

As a first observation, when increasing the depth, the PL signal decreased exponentially regardless of the wavelength collection band used as illustrated (**Figures 5a, S3).** To evaluate the impact of depth and wavelength collection on spatial resolution, a capillary tube was filled with Au NCs (45.5 µM in PBS 10 mM) and immersed at various depths in Intralipid 2%. This standard protocol is used to mimic a contrast agent circulating in a blood vessel within biological tissue *in vivo* since Intralipid 2% has been shown to display similar optical properties (µa and µs') than the human skin[29].

We considered the maximum penetration depth when SNR was > 3. Au NCs could be then detected down to 8 mm, 7 mm and 5 mm using LP1064 nm, LP1250 nm and LP1300 nm respectively (**Figure 5b**). With the LP1500 nm, the PL intensity from Au NCs in the capillary was too weak to be detected deeper than 1 mm, which was expected considering the low concentration and the PL profile of this contrast agent with signal dropping after 1400 nm.

In order to quantify the impact of scattering at different depths on the spatial resolution in the NIR-I region up to 1000 nm and at different SWIR sub-windows, we measured the variation of capillary relative width (see **Figure S5** for FWHM variations) compared to its real size (coefficient detailed in eq.1 was calculated for each condition). As illustrated in **Figure 5c**, the relative width linearly increased with depth when collecting signal in the NIR-I region. At 1 mm depth, the capillary relative width was already overestimated 5 times (2.91 mm ± 0.09 mm compared to the constructor capillary width of 0.58 mm) and this distortion highly increased with depth, leading to a blurry and undefined capillary image (9.10 mm ± 0.27 mm corresponding to a distortion to the constructor capillary width of 1569% ± 47%) at a depth of 4 mm (**Figures 5c, S6**).

In contrast, in the SWIR spectral window, no significant variation of capillary relative width was detected up to 2 mm depth, regardless of the LP used, with 103% ± 0.5%; 99% ± 0.7% and 98% ± 0.3% for LP1064 nm, LP1250 nm and LP1300 nm respectively. Above 3 mm depth, using LP1064nm, the relative width started to raise exponentially from 123% ± 1.3% at 3 mm to 1599% ± 3.4% at 7 mm. Interestingly, by selecting higher wavelength collection ranges, we noticed a reduced variation of the capillary's relative width (137% ± 7.8% and 170% ± 14.9% at 4 mm depth for LP1250 nm and LP1300 nm respectively) compared to the LP1064 nm. However, it appeared that above 4 mm even selecting sub-regions at longer wavelengths, scattering became very elevated, and led to an overestimation of the width of the capillary (**Figures 5c, S5-S7**).

4- *In vivo* vascular imaging using different SWIR sub-windows

To further investigate the influence of scattering on the empirical resolution *in vivo* in live animals, we took whole body SWIR images of a nude mouse after it received an intravenous perfusion of Au NCs in the tail vein.

The images obtained from the different SWIR sub-regions (**Figures 6a, S8-S10**) showed an obvious improvement of spatial resolution when moving towards to longer wavelengths were selected as compared to classical NIR-I imaging.

Using LP1064 nm, we observed a diffuse signal from the skin that tended to blur vessels contrast. For LP1300 nm and even more for LP1500 nm, a large number of blood vessels of heterogeneous sizes and at different depths could be detected thanks to the reduced scattering and decreasing skin auto-fluorescence. A cross-sectional profile was made through a vessels rich area to appreciate both vessels contrast and resolution using different LPs (**Figure 6a**). Although Au NCs PL decreased at the highest wavelengths, a large improvement in terms of

signal-to-noise and signal-to-skin ratios as well as spatial resolution was observed as illustrated by higher and sharper pic corresponding to blood vessels.

We then used a Monte Carlo restoration processing with an additional high pass filtering (MCR+HP filter)[20] on the previous images. As seen in **Figure 6b**, the contrast was significantly improved after processing. The comparison of the plot profiles after application of the MCR+HP filter showed narrower widths of the blood vessels, getting closer to the real sizes especially when using the LP1064 nm and LP1300 nm (**Figures 6b, S8-10**).

Discussions and conclusion

The SWIR spectral range (900-1700 nm) has recently emerged as a promising bioimaging window for non-invasive and real-time monitoring of biological processes thanks to a strong reduction of light scattering and absorption by blood and biological tissues *in vivo* resulting in significant improvement of sensitivity and spatial resolution in depth[1]. Recent studies using contrast agents such as ICG [21, 28] and IRdye800CW[28] initially designed for NIR-I imaging and commonly administered to human patients yielded dramatically augmented performances when used in SWIR imaging.

Besides, new contrast agents with high PL in the SWIR have been investigated in small animals. Among these, SWIR-emitting probes based on ultra-small gold particles (<3 nm) called Au NCs showed a high colloidal stability over several months in water and buffer solutions, exhibit high PL at wavelength above 1250 nm[18], thus making these SWIR emitters promising contrast agents. Preclinical studies in mice showed no toxicity, a good circulation time (blood half-life: $t_{1/2\alpha}$~ 0.43 h) with low nonspecific accumulation in organs and efficient renal elimination. These Au NCs have been used in *in vivo* in mice and allowed noninvasive detection of vascular disorders in bone morphogenetic protein 9 (*Bmp9*)-deficient mice[20].

In this work, we used Au NCs to investigate the impact of light scattering on the empirical spatial resolution in different SWIR sub-regions on different artificial models and in mice. Using a bright SWIR emissive composite bulk made of Au NCs and PDMS with sharp edges, we explored the scattering effects of the skin which has been identified as the main contribution to the distortion of the edge's geometry. Compare to others artificial models based on the inclusion of particles with known sizes, absorption and refractive index in medium or in tissues[30], this artificial model did not modify the sample, and in our case, the integrity of the living tissue.

We measured an overestimation of the FWHM by 113% in the presence of skin when using LP1064 nm. This overestimation was drastically reduced at higher SWIR wavelengths with a FWHM decreased by 25% between LP1064 nm and LP1500 nm. This quantitative study confirms the interest to explore NIR-IIb as the most suitable SWIR sub-region for the non-invasive exploration of living tissues. We also confirmed a decrease of scattering at longer wavelengths with a more accurate conservation of the real size of capillary immerged in a scattering medium at different depths. Indeed, we showed that below 4 mm of intralipid, the capillary width was almost half less overestimated using the LP1250 nm (137%) or LP1300 nm (170%) than with the LP1064 nm (292%).

This trend was confirmed *in vivo*. Images obtained in the 1500 – 1700 nm SWIR sub-region led to a better detection in depth, with sharper and more realistic cross-sectional profiles of the blood vessels.

In complement of the improvement that could be brought by selecting appropriate contrast agents and detection wavelengths, a major importance should be given to image treatment and restoration as a powerful tool to reduce scattering and improve biological resolution. **Figure 6b (**see also **Figures S8-10**) showed an example of contrast enhancement and spatial resolution improvement obtained with Monte Carlo restorations.

Custom-made microfluidic chips will be also highly relevant artificial models mimicking heterogeneous blood vessels in their natural environment and in the presence of blood-flow. They provide suitable systems with channels covering all the spectra of the mice vascular network, from micro-capillaries to larger vessels and provide dual information on spatial and temporal resolution.

With a NIR-IIb being an optimum SWIR sub-region, safer and brighter contrast agents in this optical window are urgently needed to demonstrate the clear breakthrough of SWIR imaging compared to NIR-I for clinical applications.

In conclusion, we showed the significant reduction of scattering from endogenous tissues at longer wavelengths in the SWIR window, using two artificial models and in small animal. Our results highlighted the necessity to develop contrast agents with strong brightness in the last and most promising SWIR window (1500-1700 nm) also called NIR-IIb. The combination of long wavelengths SWIR imaging, imaging processing and restoration allows moving non-invasive optical imaging one-step forward toward the generation of powerful tools for optical imaging adapted to the clinical practice.

Acknowledgements

We would like to thank Cancéropôle Lyon Auvergne Rhône-Alpes (CLARA), ITMO Cancer Aviesan program "Equipment" of Plan Cancer III (2017), Plan Cancer (C18038CS), and the Foundation ARC (R17157CC) for their financial support. The Optimal imaging platform is supported by France Life Imaging (French program "Investissement d'Avenir" grant; "Infrastructure d'avenir en Biologie Santé", ANR-11-INBS-0006) and the IBISA French consortium "Infrastructures en Biologie Santé et Agronomie".

References

1. G. Hong, A. Antaris and H. Dai, *Nature biomedical engineering*, 2017, **1**, 0010 (0011-0022).
2. Z. Hu, C. Fang, B. Li, Z. Zhang, C. Cao, M. Cai, S. Su, X. Sun, X. Shi, C. Li, T. Zhou, Y. Zhang, C. Chi, P. He, X. Xia, Y. Chen, S. S. Gambhir, Z. Cheng and J. Tian, *Nature Biomedical Engineering*, 2020, **4**, 259-271.
3. B. Kahramangil and E. Berber, *Journal of Surgical Oncology*, 2017, **115**, 848-855.
4. M. Koch, P. Symvoulidis and V. Ntziachristos, *Nature Photonics*, 2018, **12**, 505-515.
5. J. Zhao, D. Zhong and S. Zhou, *Journal of Materials Chemistry B*, 2018, **6**, 349-365.
6. L.-Y. Huang, S. Zhu, R. Cui and M. Zhang, *Analytical Chemistry*, 2020, **92**, 535-542.
7. G. Hong, S. Diao, J. Chang, A. L. Antaris, C. Chen, B. Zhang, S. Zhao, D. N. Atochin, P. L. Huang, K. I. Andreasson, C. J. Kuo and H. Dai, *Nature Photonics*, 2014, **8**, 723-730.
8. Y. Zhang, Y. Zhang, G. Hong, W. He, K. Zhou, K. Yang, F. Li, G. Chen, Z. Liu, H. Dai and Q. Wang, *Biomaterials*, 2013, **34**, 3639-3646.
9. J. T. Robinson, G. Hong, Y. Liang, B. Zhang, O. K. Yaghi and H. Dai, *Journal of the American Chemical Society*, 2012, **134**, 10664-10669.
10. G. Hong, J. C. Lee, J. T. Robinson, U. Raaz, L. Xie, N. F. Huang, J. P. Cooke and H. Dai, *Nature Medicine*, 2012, **18**, 1841-1846.
11. S. S. Kang, D.-M. Geum, K. Kwak, J.-H. Kang, C.-H. Shim, H. Hyun, S. H. Kim, W. J. Choi, S.-H. Choi, M.-C. Park and J. D. Song, *Scientific Reports*, 2019, **9**, 12875.
12. Q. Yang, Z. Ma, H. Wang, B. Zhou, S. Zhu, Y. Zhong, J. Wang, H. Wan, A. Antaris, R. Ma, X. Zhang, J. Yang, X. Zhang, H. Sun, W. Liu, Y. Liang and H. Dai, *Advanced Materials*, 2017, **29**, 1605497.
13. M. Zhang, J. Yue, R. Cui, Z. Ma, H. Wan, F. Wang, S. Zhu, Y. Zhou, Y. Kuang, Y. Zhong, D.-W. Pang and H. Dai, *Proceedings of the National Academy of Sciences*, 2018, **115**, 6590.
14. Y. Zhang, G. Hong, Y. Zhang, G. Chen, F. Li, H. Dai and Q. Wang, *ACS Nano*, 2012, **6**, 3695-3702.
15. D. Franke, D. K. Harris, O. Chen, O. T. Bruns, J. A. Carr, M. W. B. Wilson and M. G. Bawendi, *Nature Communications*, 2016, **7**, 12749.
16. D. J. Naczynski, M. C. Tan, M. Zevon, B. Wall, J. Kohl, A. Kulesa, S. Chen, C. M. Roth, R. E. Riman and P. V. Moghe, *Nature Communications*, 2013, **4**, 2199.
17. S. Ding, L. Lu, Y. Fan and F. Zhang, *Journal of Rare Earths*, 2020, DOI: https://doi.org/10.1016/j.jre.2020.01.021.

18. Y. Chen, D. Montana, H. Wei, J. Cordero, M. Schneider, X. Le Guevel, O. Chen, O. Bruns and M. Bawendi, *Nanoletters*, 2017, **17**, 6330-6334.
19. B. Musnier, K. D. Wegner, C. Comby-Zerbino, V. Trouillet, M. Jourdan, I. Hausler, R. Antoine, J. L. Coll, U. Resch-Genger and X. Le Guevel, *Nanoscale*, 2019, **11**, 12092-12096.
20. Z. Yu, B. Musnier, K. D. Wegner, M. Henry, B. Chovelon, A. Desroches-Castan, A. Fertin, U. Resch-Genger, S. Bailly, J.-L. Coll, Y. Usson, v. josserand and X. Le Guével, *ACS Nano*, 2020, **14**, 4973-4981.
21. J. A. Carr, D. Franke, J. R. Caram, C. F. Perkinson, M. Saif, V. Askoxylakis, M. Datta, D. Fukumura, R. K. Jain, M. G. Bawendi and O. T. Bruns, *Proceedings of the National Academy of Sciences of the United States of America*, 2018, **115**, 4465-4470.
22. S. Zhu, Z. Hu, R. Tian, B. C. Yung, Q. Yang, S. Zhao, D. O. Kiesewetter, G. Niu, H. Sun, A. L. Antaris and X. Chen, *Advanced Materials*, 2018, **30**, 1802546.
23. S. Zhu, B. C. Yung, S. Chandra, G. Niu, A. L. Antaris and X. Chen, *Theranostics*, 2018, **8**, 4141-4151.
24. K. Welsher, S. P. Sherlock and H. Dai, *Proceedings of the National Academy of Sciences*, 2011, **108**, 8943.
25. S. Ali and B. Wesam, *Polish Journal of Medical Physics and Engineering*, 2017, **23**, 121-126.
26. R. R. Zhang, A. B. Schroeder, J. J. Grudzinski, E. L. Rosenthal, J. M. Warram, A. N. Pinchuk, K. W. Eliceiri, J. S. Kuo and J. P. Weichert, *Nature Reviews Clinical Oncology*, 2017, **14**, 347-364.
27. J.-B. Li, H.-W. Liu, T. Fu, R. Wang, X.-B. Zhang and W. Tan, *Trends in Chemistry*, 2019, **1**, 224-234.
28. Z. Starosolski, R. Bhavane, K. B. Ghaghada, S. A. Vasudevan, A. Kaay and A. Annapragada, *PLOS ONE*, 2017, **12**, e0187563.
29. L. T. Tamara and N. T. Suresh, *Journal of Biomedical Optics*, 2001, **6**, 167-176.
30. J. D. Rogers, A. J. Radosevich, J. Yi and V. Backman, *IEEE Journal of Selected Topics in Quantum Electronics*, 2014, **20**, 173-186.

a

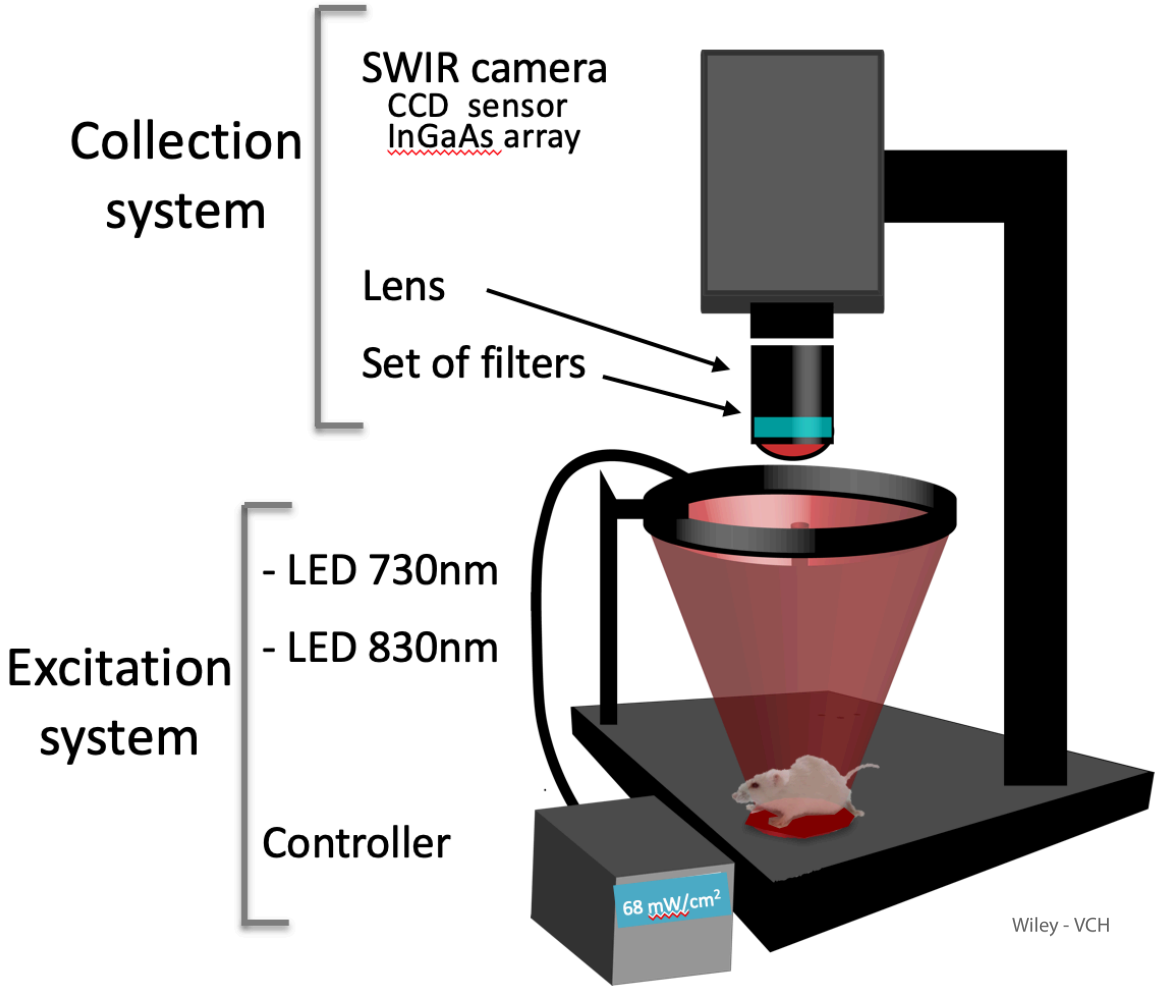

b

Excitation source	λ= 730 nm	λ= 830 nm
Power density (mW/cm^2)	16	68
Irradiation area (cm^2)	30	23

c

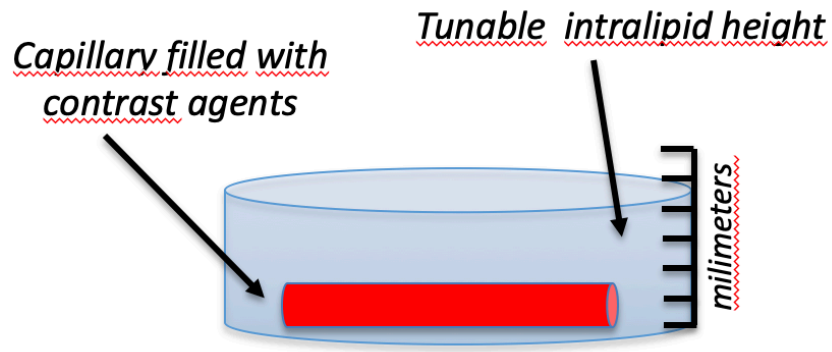

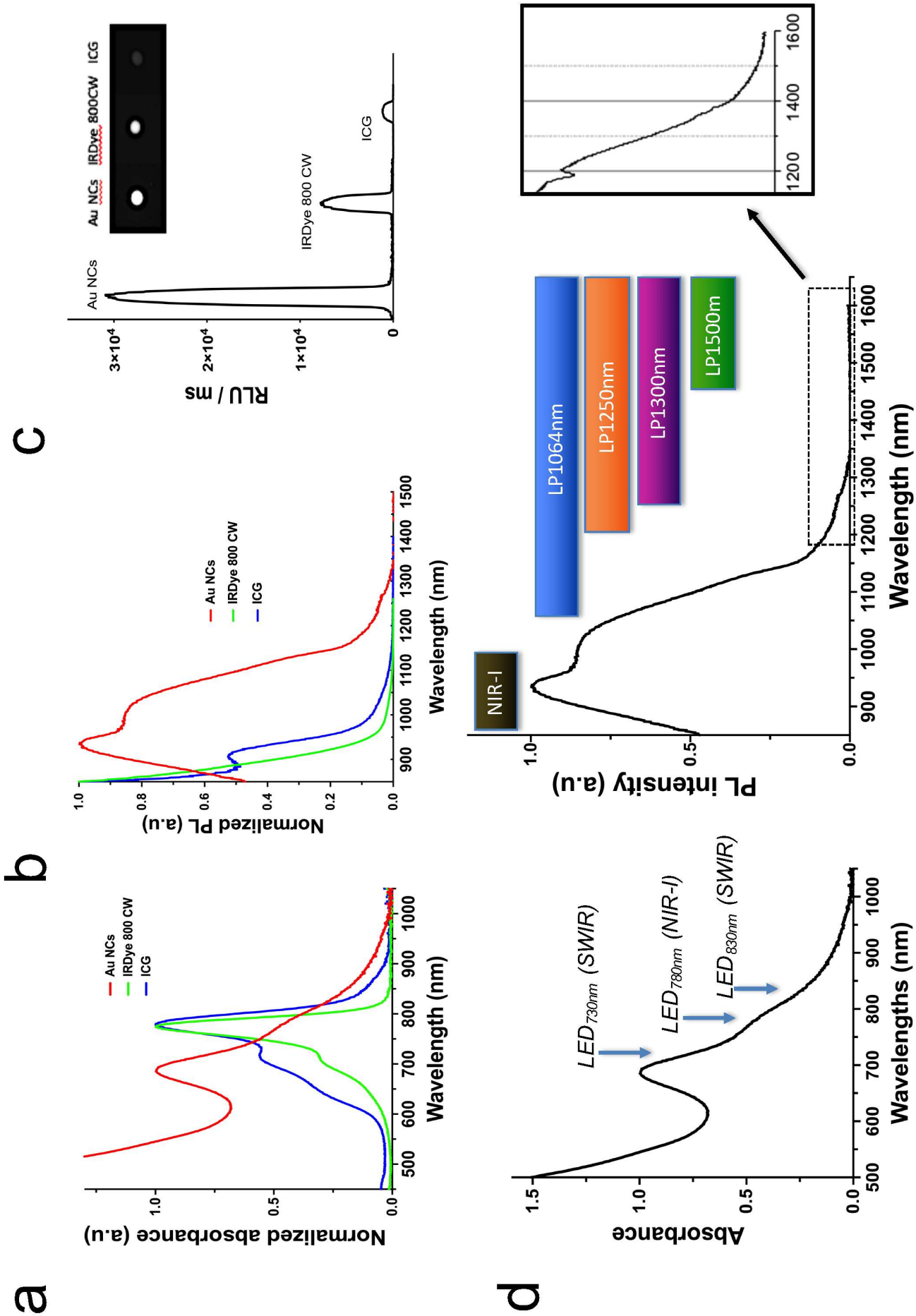
a
Normalized absorbance (a.u)
Wavelength (nm)
Au NCs
IRDye 800 CW
ICG
b
Normalized PL (a.u)
Wavelength (nm)
Au NCs
IRDye 800 CW
ICG
c
RLU / ms
Au NCs
IRDye 800 CW
ICG
Au NCs
IRDye 800CW
ICG
d
Absorbance
Wavelengths (nm)
LED730nm (SWIR)
LED780nm (NIR-I)
LED830nm (SWIR)
PL intensity (a.u)
Wavelength (nm)
NIR-I
LP1064nm
LP1250nm
LP1300nm
LP1500m

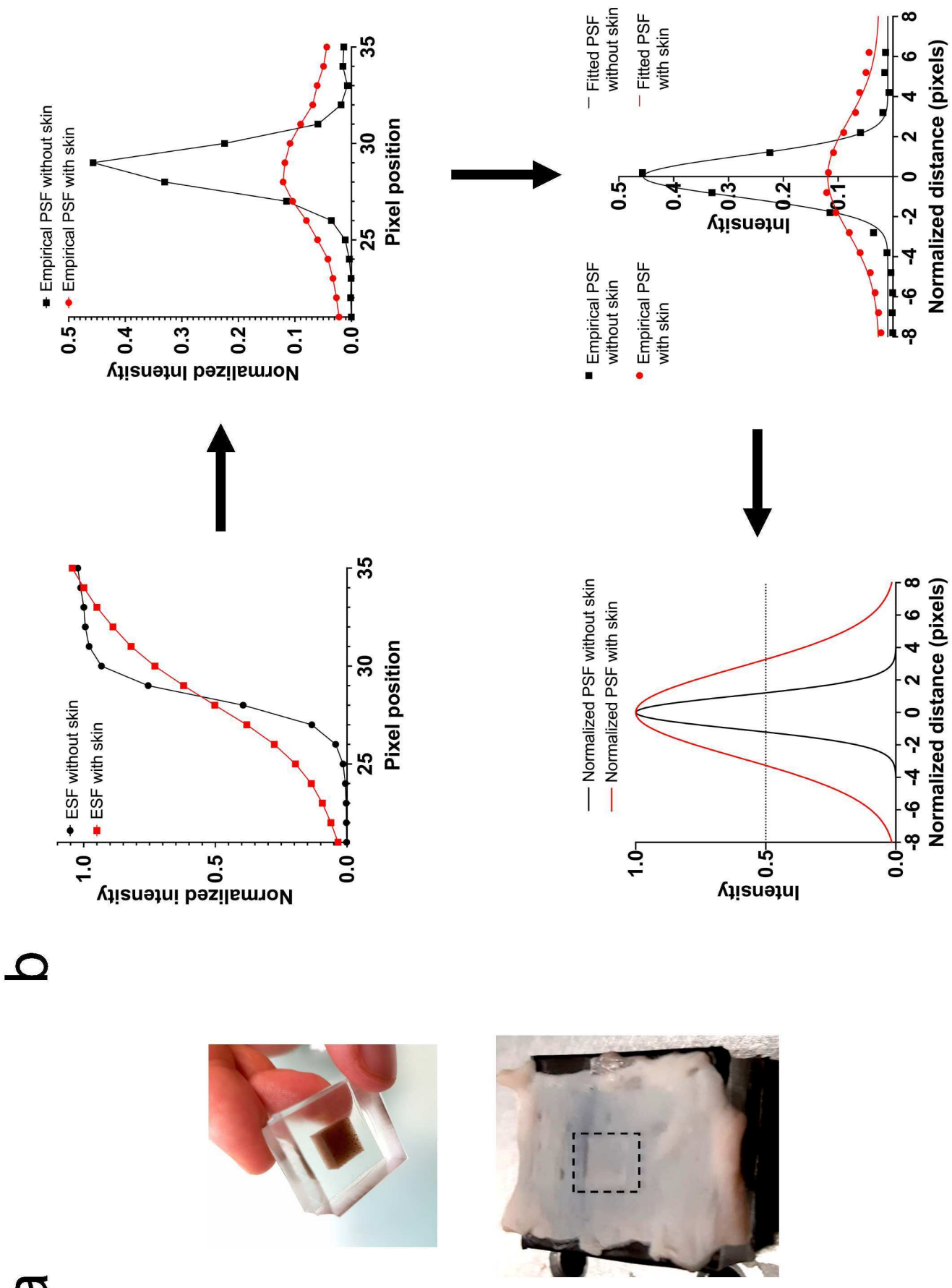

Figure 3. (a). Au NCs/PDMS composite with skin flab from BALB/c nude mice. (b). Steps for scattering normalized PSF determination using the composite Au NCs / PDMS artificial model.

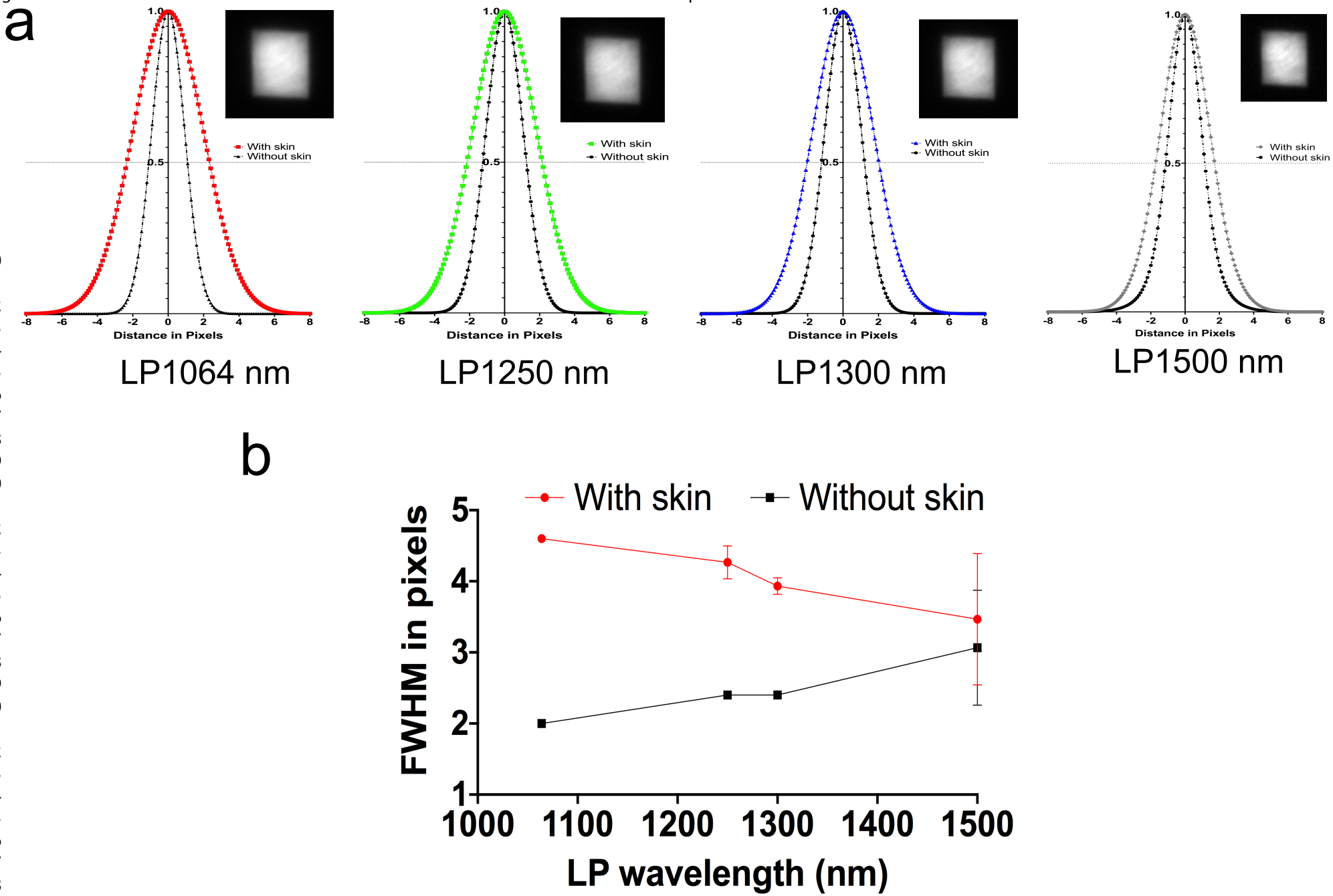

Figure 4. (a) Normalized PSF and images of Composite PDMS / Au NCs artificial model covered by skin using different SWIR LPs. (b) FWHM of Normalized PSF of Composite Au NCs / PMDS artificial model covered and unvovered by mouse skin using different SWIR sub-windows.

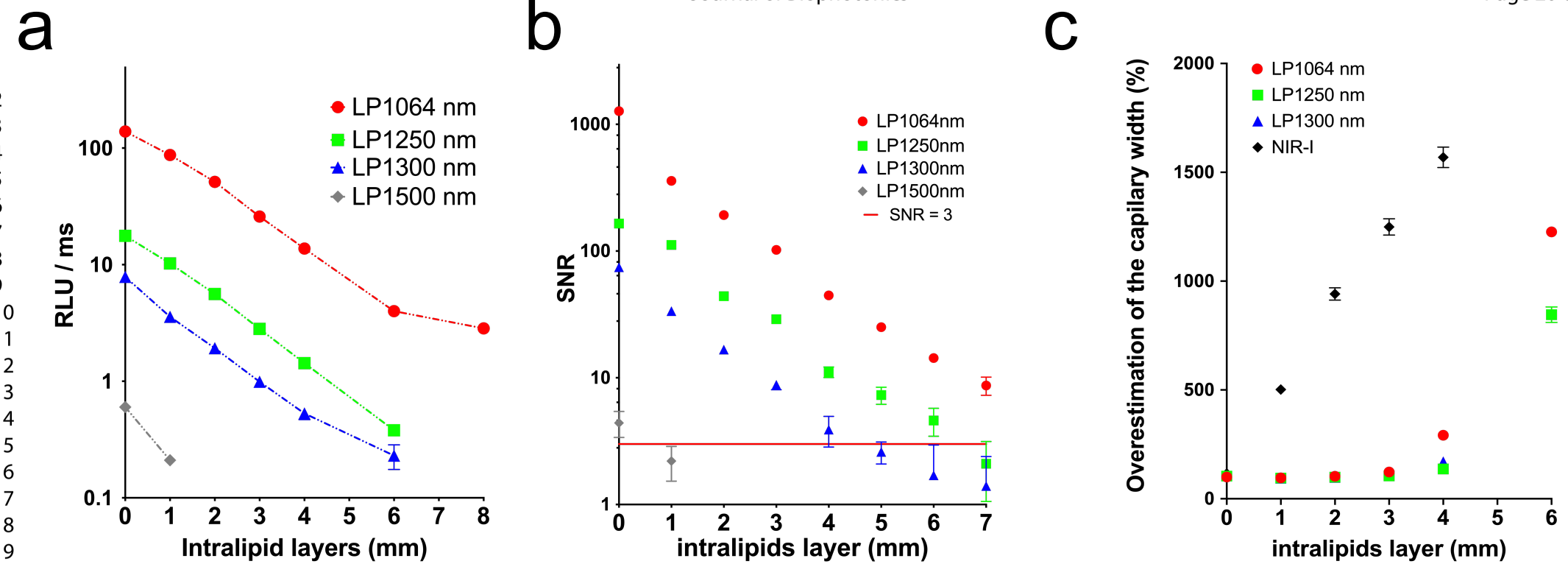

Figure 5. (a) Logarithmic scale intensity profiles under different intralipid height using different SWIR LPs for Au NCs. $\lambda_{exc.}$ 830 nm. (b) Logarithmic representation of Signal to Noise Ratio of Au NCs contrast agent using different SWIR LPs as a function of the intralipid height and (c) Comparison between FWHM of cross-sectional profiles in capillary images and constructor capillary's width in different SWIR sub windows and for NIR-I.

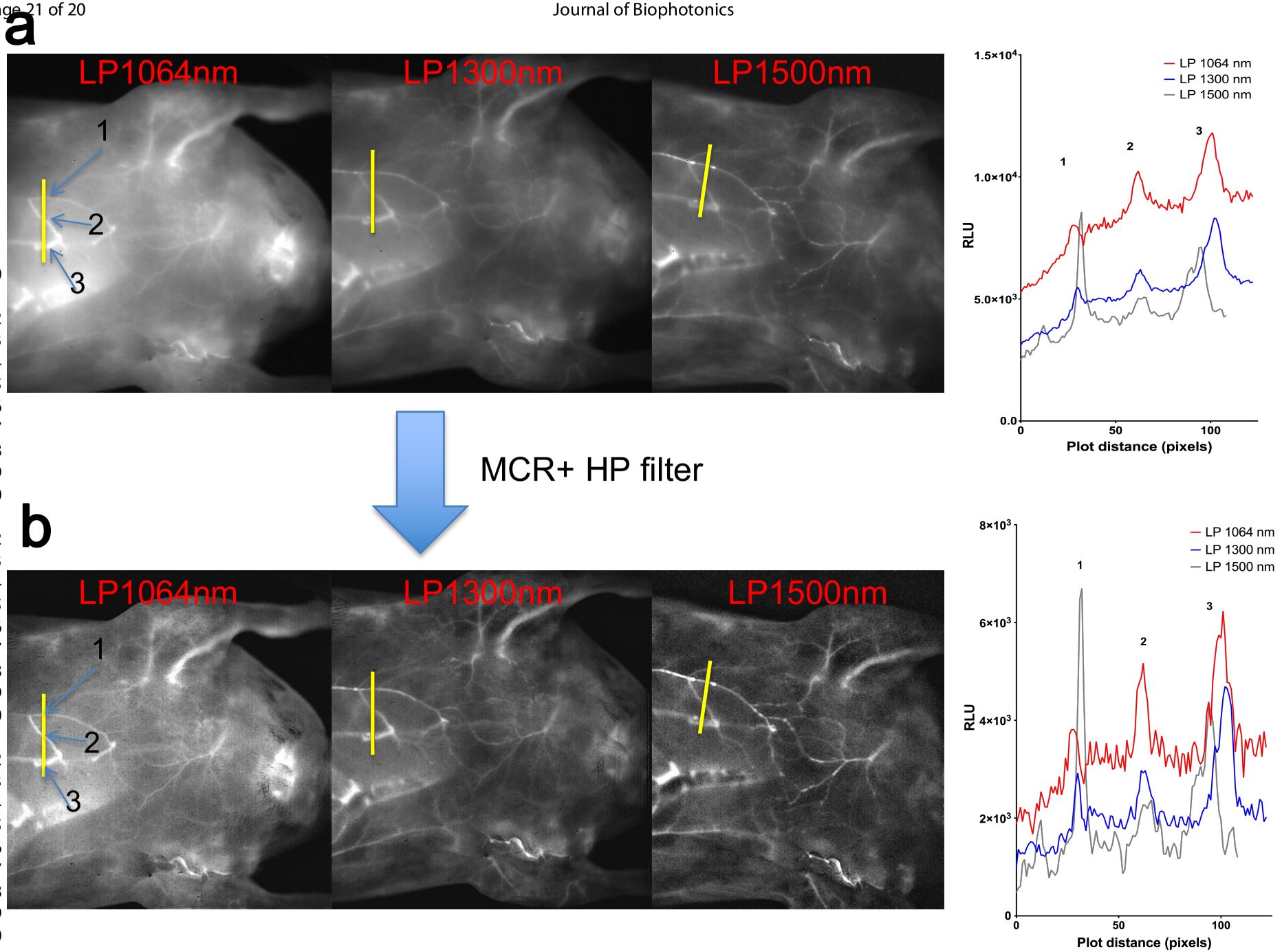

Figure 6. *In vivo* vascular imaging and cross-sectional plot profiles of ventral blood vessels after i.v. injection of Au NCs using LP1064 nm, LP1300 nm, LP1500 nm (a) before and (b) after Monte Carlo constrained restoration with an additional filtering (MCR+HP filter).